Integrated Optical-Wireless Interface and Detection

Chapter 7
Integrated Optical-Wireless Interface and Detection

Dimitrios Konstantinou, Lei Xue, Tanjil Shivan, Maruf Hossain, Simon Rommel, Ulf Johannsen, Christophe Caillaud, Viktor Krozer, Jiajia Chen, and Idelfonso Tafur Monroy

Abstract This chapter elaborates on the beneficial aspects and hardware implementations of incorporating ultradense WDM-PONs (UDWDM-PONs) with hybrid optical-wireless fronthaul links and fiber to the home applications. Simulation results on the synthesis of a low-cost and low-energy consumption optoelectronic unit within the future 5G base stations (BS) are presented. In addition, an advanced neural network is investigated capable of compensating for the linear and nonlinear effects induced by semiconductor optical amplifiers (SOA).

7.1 Introduction

Passive optical networks (PONs) are associated with fiber to the home (FTTH) connections providing broadband and high-speed communications. Due to the emergence of new technologies, a large amount of consumer and business use cases that need to be supported by PONs demand the migration from the existing WDM-PONs to ultradense WDM-PONs within urban areas. Moreover, in the wireless domain, the dawn of 5G had provided the impetus for future radio access networks to support 1000 times more capacity enabling high-speed connections to a huge

D. Konstantinou (✉) · S. Rommel · U. Johannsen · I. T. Monroy
Eindhoven University of Technology, Eindhoven, The Netherlands
e-mail: d.konstantinou@tue.nl

L. Xue · J. Chen
Chalmers University of Technology, Göteborg, Sweden
e-mail: leixu@chalmers.se

T. Shivan · M. Hossain · V. Krozer
Ferdinand-Braun-Institut, Leibniz-Institut für Höchstfrequenztechnik (FBH), Berlin, Germany
e-mail: Tanjil.Shivan@fbh-berlin.de

C. Caillaud
III-V Lab (A Joint Laboratory Between Nokia Bell Labs, Thales R&T and CEA Leti), Palaiseau, France
e-mail: christophe.caillaud@3-5lab.fr

J. Rodriguez et al. (eds.), *Enabling 6G Mobile Networks*,
https://doi.org/10.1007/978-3-030-74648-3_7

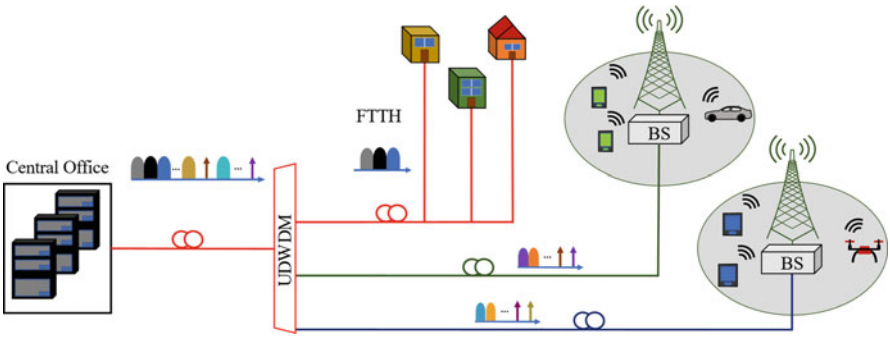

Fig. 7.1 A block diagram of the network proposed by the European ITN project 5G STEP FWD. Optical signals spaced within the UDWDM grid serve different applications such as FTTH, as well as mm-wave wireless access to various end-user applications such as autonomous vehicular communications

amount of users in a dense environment with guaranteed quality of service and exceptionally low latency [1]. A dynamic way to achieve these aforementioned requirements is by employing hybrid photonic-wireless links operating in the lightly licensed millimeter-wave (mm-wave) bands that are integrated with the UDWDM-PONs.

The core concept presented in this chapter is illustrated in Fig. 7.1. At the central office (CO), the optical signal generation and multiplexing will take place. The resource management and allocation within the UDWDM-PON are offered by a centralized control plane defined by the network function virtualization (NFV) and software-defined networking (SDN). This leads to a more flexible routing allowing the reduction of the network's complexity increasing control and minimizing the communications latency. Moreover, combining analogue radio over fiber (ARoF) fronthaul with flexible carrier aggregation allows optimum resource utilization. In the optical domain, 5G New Radio (NR) modulated signals, and signals for FTTH (e.g., NRZ, PAM4) propagate within the UDWDM-PON toward their designated terminal (5G base stations or homes, respectively) through the support provided by a UDWDM de-multiplexer that contributes to the separation of these optical waves [2]. Since optical heterodyning will be employed for the mm-wave generation within the future 5G base stations, unmodulated local oscillators are also multiplexed with the rest of the optical signals at the central office [3]. The remainder of this chapter aims to provide solutions toward the integration of optoelectronic integrated components within the 5G base stations, as well as to present digital signal processing techniques to mitigate distortions caused to FTTH signals by the passive optical network.

Within Sect. 7.2, the physical concepts describing optical heterodyning and the operation of uni-travelling carrier photodiodes (UTC-PDs) are explained. Moreover, the processes on the acquisition of the full-equivalent circuit of these devices are

analyzed by using both simulation tools and mathematical equations. Furthermore, the properties of transimpedance amplifiers (TIAs) are explained in terms of gain and noise. Finally, the results of a co-simulation between a UTC-PD and a multistage TIA operating in V-band are discussed underlining all the important aspects of high-speed, high-gain optoelectronic co-integration.

For FTTH applications, the advanced 25G avalanche photodiodes with high sensitivity are costly in the passive optical networks. Thus, the combination of semiconductor optical amplifiers (SOA) used as pre-amplifier with photodiodes (PD) is proposed as a low-cost solution to improve system power budget. However, the SOA nonlinearities due to the gain saturation, e.g., the pattern effect, degrade the system performance significantly that increasingly worsen with increasing system speed. Thus, digital signal processing (DSP) is often used as a powerful tool and combined with the use of a neural network to compensate the linear and nonlinear distortions. The performance of NN is investigated in Sect. 7.3 within an intensity modulation with direct detection (IM/DD) system, with 50G PAM4 signals showcasing the nonlinearity compensation and receiver dynamic range improvement.

7.2 Hybrid Photonic-Wireless Interface Unit for 5G Base Stations

The interface between optics and RF high-speed electronics will take place at the 5G base stations of Fig. 7.2. Channel interleaving controlled by the SDN/NFV plane and de-multiplexing (DeMUX) will guarantee that each modulated optical signal is matched to an unmodulated tone (LO) such that their frequency distance is equivalent to the desired RF carrier frequency of the mm-wave.

Each output of the DeMUX will provide input to integrated photonic-wireless transmitting units. Such units are novel photonic-wireless chip interfaces comprising high-speed photodiodes and RF electronic circuits. Uni-travelling carrier photodiodes (UTC-PDs) are promising candidates for the conversion of optical signals to mm-waves through optical heterodyning [4, 5]. The generated mm-waves will be amplified by broadband and high-gain integrated transimpedance amplifiers (TIAs) and transmitted in the wireless domain by mm-wave antennas [6].

The wireless operation in the mm-wave bands supports the transmission using wide wireless channels that are capable of providing peak user data rates in the Gbit/s range. The use of traditional methods for digitized fronthaul and electrical up-conversion of baseband signals to mm-wave frequencies is limited to narrow bandwidth signals not appropriate for high data throughput. Therefore, the signal up-conversion through optical heterodyning and analogue radio over fiber has become a promising solution.

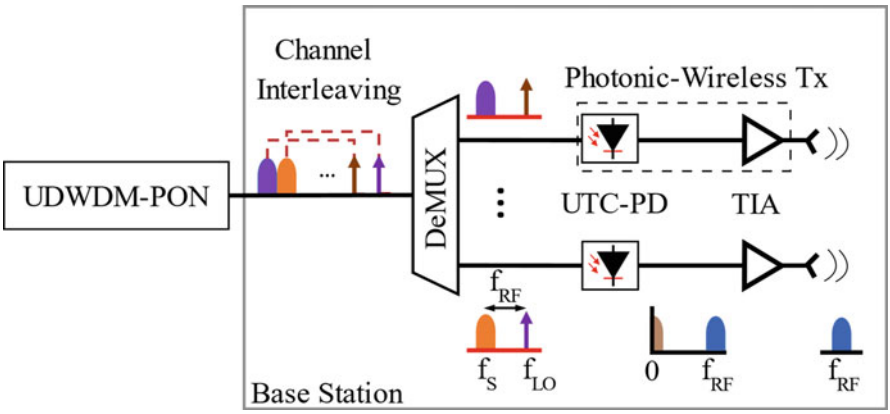

Fig. 7.2 A base station fed by UDWDM-PON where the mm-wave generation and transmission are conducted by photonic-wireless integrated chips that include high-speed UTC-PDs, TIAs, and antenna elements

7.2.1 Optical Heterodyning for mm-wave Generation

The millimeter-wave generation in the optical domain has been widely studied and is based on optical heterodyning, i.e., the beating of two optical signals spaced at a desired RF frequency ($f_{RF} = f_{LO} - f_S$) on a photodiode.

The derivations describing this physical concept are analyzed based on mathematical calculations. As shown at the bottom of Fig. 7.2, the electric fields for both the signal ($\boldsymbol{E_s}$) carrying modulated data and a local oscillator ($\boldsymbol{E_{LO}}$) can be expressed in (7.1) [7] as

$$\boldsymbol{E_s}(t) = \sqrt{P_s}s(t)e^{-i(\omega_s t+\phi_s)}$$

$$\boldsymbol{E_{LO}}(t) = \sqrt{P_{LO}}e^{-i(\omega_{LO} t+\phi_{LO})} \tag{7.1}$$

where $s(t)$ is the modulated signal in baseband and P_s, P_{LO} are the optical signal powers. Both electric fields oscillate at radial frequencies ω_s, ω_{LO} and carry phase components ϕ_s, ϕ_{LO}, which depend mostly on the properties of the sources used (e.g., laser linewidth). Moreover, the local oscillator (LO) is a co-propagating optical tone that carries no modulation.

Typically, in electronic mixers, LO signals are special as these are driving the nonlinear device (i.e., mixer) into large-signal excitation and the RF signal that is up-/down-converted assumed being small, giving rise to a linearized periodic circuit. This is not the case in optical heterodyning within photodiodes.

Thus, assuming that both fields are co-polarized, the electric field at the photodiode ($\boldsymbol{E_{PD}}$) is calculated in (7.2):

$$\begin{aligned} \boldsymbol{E}_{PD} &\propto |\boldsymbol{E}_s(t) + \boldsymbol{E}_{LO}(t)|^2 \\ &= [\boldsymbol{E}_s(t) + \boldsymbol{E}_{LO}(t)]\overline{[\boldsymbol{E}_s(t) + \boldsymbol{E}_{LO}(t)]} \\ &= |\boldsymbol{E}_s(t)|^2 + |\boldsymbol{E}_{LO}(t)|^2 + \boldsymbol{E}_s(t)\overline{\boldsymbol{E}_{LO}(t)} + \overline{\boldsymbol{E}_s(t)}\boldsymbol{E}_{LO}(t) \\ &= P_s s^2(t) + P_{LO} + 2\sqrt{P_s P_{LO}} s(t)\ \cos(\omega_{RF} t + \phi_{RF}) \end{aligned} \tag{7.2}$$

with the desired RF signal given as $2\sqrt{P_s P_{LO}} s(t)\ \cos(\omega_{RF} t + \phi_{RF})$. The components $P_s s^2(t) + P_{LO}$ are filtered out by the waveguide connected to the mm-wave antenna.

Therefore, the optical heterodyning of two optical tones is an efficient and simple way to generate mm-wave signals. This process is commonly referred to as photonic up-conversion since any modulation present on the optical signals is transferred in the RF domain. Furthermore, this process allows the simplification of the wireless transmitters since no high-frequency sources are needed at the base stations to electrically up-convert the signals. Finally, since the LOs are generated at the central office, the total network topology is even more centralized, and the costs of the base stations are reduced even further.

7.2.2 *Physical Properties of Photodiodes*

In order to thoroughly comprehend the mm-wave generation based on optical heterodyning, it is essential for the reader to grasp the physical properties and functionalities of photodiodes. In principle, once photons are absorbed by a PD, electron-hole pairs are generated and travel through its junction. There are different methods for coupling light to the absorption layer of a PD such as the evanescent coupling [8] that is illustrated in Fig. 7.3a. In this case, light propagating through the optical waveguide is gradually absorbed by the carrier generation layer.

One example of such optoelectronic structure is the PIN photodiode of Fig. 7.3b that consists of three different types of semiconductor materials: an intrinsic region that acts as the carrier generation layer once the absorbed photons have energy

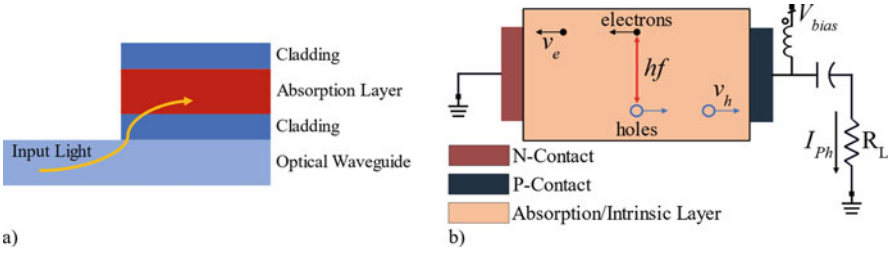

Fig. 7.3 (**a**) A block diagram depicting the evanescent coupling of light to the absorption region of PDs; (**b**) A PIN-PD capable of generating current at its load RL due to the creation of electron-hole pairs by the absorption of photons with energy hf

($E = hf$) higher than its bandgap, a P-type semiconductor collecting the generated holes, and an N-type material attracting the electrons [9]. If an adequate reverse bias (V_{bias}) is applied, the intrinsic region becomes fully depleted, and a strong electric field is established across the junction accumulating the photogenerated carriers that drift toward the contacts of the device inducing a photocurrent (I_{ph}) at its load (R_L).

A fundamental parameter of a PD is its responsivity (R_{opt}), calculating the ratio of the flux of generated electrical carrier over the one of incident photons. Therefore, the responsivity is given as the ratio of I_{ph}/P_{opt} and is measured in A/W. Moreover, except for the generated photocurrent, there is an additional noise parameter that is due to the random generation and annihilation of charges within the depletion region of the PD. This noise source is defined as dark current (I_{dark}), and its amplitude resides within the range of nA.

Apart from the abovementioned static parameters of a photodiode, the response of the device over frequency is also critical. The 3 dB bandwidth (f_{3dB}) of a PD consists of two elements. The first is determined by the RC time constant (τ_{RC}) of the device that depends on the total resistance (R) and capacitance (C) of the PD including its junction capacitance (C_j), its series resistance (R_s), and all the parasitics added from the transmission line (TML). The second element of (7.3) depends on the transit time (τ_{tr}) of the carriers generated in the absorption layer. This parameter varies based on the type of the PD and the speed of the generated electrons (v_e) and holes (v_h). Since $v_e > v_h$ [10], the transit time of the holes within the device defines its speed.

$$f_{3dB} = \sqrt{\frac{1}{\frac{1}{f_{RC}^2} + \frac{1}{f_{tr}^2}}},\ f_{RC} = \frac{1}{2\pi\tau_{RC}} = \frac{1}{2\pi RC},\ f_{tr} = \frac{1}{2\pi\tau_{tr}} \tag{7.3}$$

Except for the PIN-PDs, avalanche photodiodes (APDs) are used in telecommunication systems. APDs contain an avalanche multiplication layer neighboring the absorption region where a single photon produces hundreds of electron-hole pairs leading to an amplification factor [11]. However, these devices are limited in terms of noise and bandwidth comparing to uni-travelling carrier photodiodes (UTC-PDs) that show great potential in terms of power and speed [12].

7.2.3 The Uni-travelling Carrier Photodiode (UTC-PD)

A uni-travelling carrier photodiode (UTC-PD) is an example of a high-speed photodetecting device providing increased sensitivity, broad bandwidth, and high saturation powers.

A block diagram of the overall structure of a UTC-PD is presented in Fig. 7.4. The carrier generation takes place at a thin absorption layer [13]. In addition, a diffusion block layer supports the unidirectional motion of electrons toward the

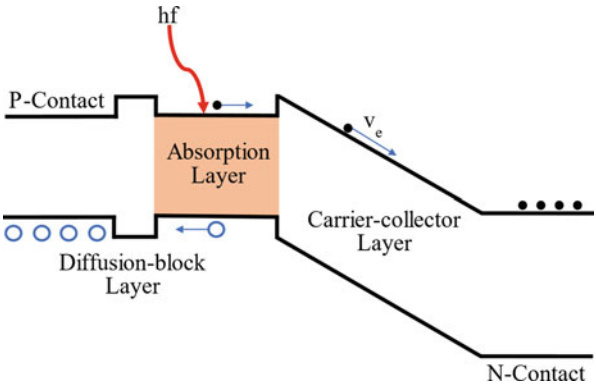

Fig. 7.4 A block diagram showing the different semiconductor material layers within a UTC-PD and the carrier generation while photons are absorbed

N-Contact. The holes are directly swept at the P-Contact within the dielectric relaxation time of the P-doped layer (>THz bandwidth). Thus, the transit time of the device (τ_{tr}) is mainly limited by the speed of the electrons within the total structure from the absorption region to the carrier-collector layer to the N-Contact. Since the velocity of the electrons in the carrier-collector layer is much higher than the velocity of the holes in the absorption layer, the bandwidth of these devices is higher than the traditional PIN-PDs.

Concerning the experimental characterization of UTC-PDs, there are various parameters that can be investigated such as responsivity and dark current measurement in the DC domain or RF saturation powers and 3 dB bandwidth. Moreover, an important characterization process is the measurement of the reflection coefficients of a UTC-PD with a vector network analyzer (VNA) and its correlation with lumped electronic elements.

7.2.3.1 Synthesis of the Equivalent Circuit of UTC-PDs

The measurement of the equivalent circuit of the diodes is of utmost importance since they provide crucial information about their physical properties and limitations. Therefore, it is imperative that the S-parameters of the device are measured.

Hence, as shown in Fig. 7.5a, a VNA is used to extract the reflection coefficients (S_{11}) of the waveguide pad structures (open and short) as well as the UTC-PDs of Fig. 7.5b. An essential component for this measurement is the RF probe touching the pads of the diode. Between the RF probe and the VNA, a power supply is connected providing a reverse bias to the diodes under test. Within the VNA, an internal bias tee is responsible for the isolation of the DC photocurrent generated by the photodiode allowing only the RF signal to be received.

A sample of the S_{11} parameters that are obtained for the measurements of open (OC) and short (SC) on-wafer structures as well as for a UTC-PD at an applied bias of -3 V is depicted in Fig. 7.6a, b. It can be observed that the curvature of the short circuit pad has an inductive behavior, and therefore the measured waveguide

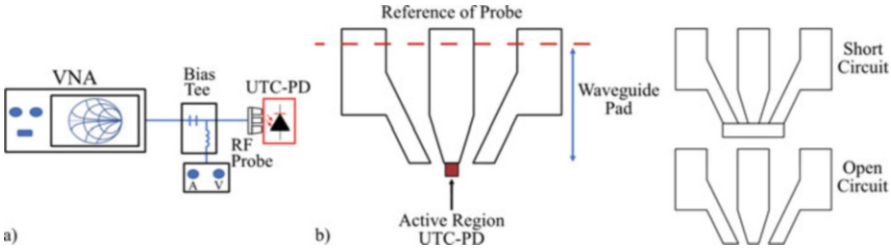

Fig. 7.5 (**a**) The measurement setup extracting the S_{11} parameters of UTC-PDs; (**b**) The UTC-PD, open and short on-wafer structures used for measurements of reflection coefficient parameters

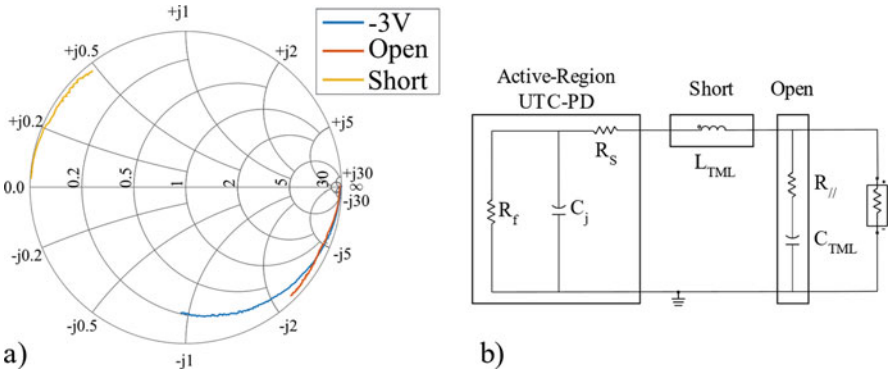

Fig. 7.6 (**a**) The Smith charts of the S_{11} parameters for the open and short waveguide as well as for a $4 \times 20\ \mu m^2$; (**b**) The lumped equivalent circuit in ADS of a photodiode based on S_{11} parameters

parameters can be matched with an inductor (L_{TML}). The similar process models the open circuit that has a capacitance (C_{TML}). Moreover, a resistor ($R_{//}$) is added in series to C_{TML} to correct for the non-ideal performance of the open structure (e.g., potential leakage to substrate) [14]. In some cases, $R_{//}$ is small and can be omitted. Then, the junction capacitance (C_j) and series resistance (R_S) within the active region of the UTC-PDs are calculated. Finally, a parasitic resistor is shunt (R_f) in parallel to (C_j) achieving a perfect matching between the model and the measurements. In the majority of the models, the (R_f) is calculated to be very high (within $k\Omega$), and this parallel branch can be considered as open. The extraction of the components synthesizing the equivalent circuit can be achieved either by using a circuit design software such as ADS [15] by Keysight or analytically through mathematical derivations.

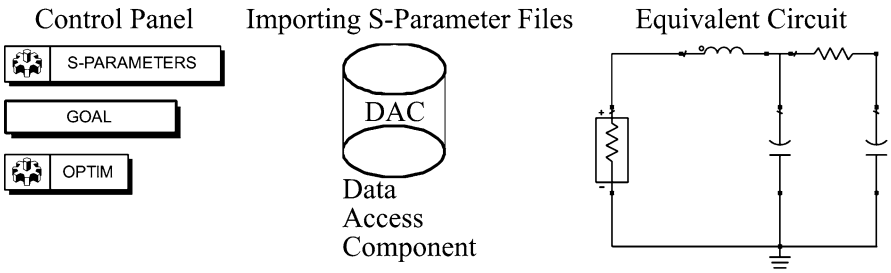

Fig. 7.7 An overview for the simulation in ADS of a lumped circuit based on obtained S_{11} parameters

Table 7.1 The values of the lumped components for the full equivalent simulation of a $4 \times 20\ \mu m^2$ UTC-PD at a reverse bias of bias of 3 V

Symbol	Description	Value
C_{TML}	TML capacitance	21.26 fF
$R_{//}$	TML resistor	1.27 Ω
L_{TML}	TML inductance	55.63 pH
C_j	Junction capacitance	24.16 fF
R_S	Series resistance	24.33 Ω
R_f	Parasitic resistance	3.61 kΩ

Extraction of Equivalent Circuit Parameters with ADS

An example of the processes followed in the software environment of ADS is illustrated in Fig. 7.7. The measured (S_{11}) data are imported to the software in the .s2p file form through an S-parameter reading block. In the next step, a circuit based on lumped components is composed.

Furthermore, the S-parameters of the measured structures (S_{meas}) are matched with the parameters of the model (S_{model}) using the optimization tool of ADS. The optimum point is achieved when the error (ϵ) margin defined by (7.4) is minimized and within the objective range defined. Once the optimization is finalized, the values of the lumped components are automatically updated.

$$\epsilon = \frac{|S_{meas} - S_{model}|}{|S_{meas}|} * 100\% \tag{7.4}$$

The percentage of the error calculation derived from the extraction of the equivalent circuit based on the data for the short, open, and UTC-PD structures is below 5%, confirming that a lumped element equivalent circuit can be synthesized based on reflection coefficient measurements with high accuracy. The values of the lumped elements can be observed in Table 7.1. However, due to the linear nature of the equivalent circuit, the optimized lumped element values in the circuit are not unique.

Analytical Extraction of Equivalent Circuit Parameters

An alternative to the abovementioned method is the calculation of the lumped components through asymptotic equations based on the measured reflection coefficient data. As a first step, all the measured reflection coefficient parameters are translated into impedances, and the parameters of the waveguide are calculated based on (7.5), which are determined from the open circuit measurement as

$$\mathrm{Z}_{meas} = \mathrm{Z}_0 \frac{1 + \mathrm{S}_{meas}}{1 - \mathrm{S}_{meas}}$$

$$C_{TML} = \frac{1}{j\omega Z_{OC}}, L_{TML} = \frac{Z_{SC}}{j\omega} \tag{7.5}$$

It is derived that $C_{TML} = 22.7$ fF and $L_{TML} = 55.2$ pH that differ from the ADS simulation results by 5.7% and 0.7%, respectively.

Then by calculating Z_{Series}, all the parallel components added to the UTC-PD by the transmission lines are removed without taking into account the additional inductors and resistors. Then C_j and R_s can be obtained from (7.6) that is based on the previous calculations.

$$Z_{Series} = \left({Z_{meas}}^{-1} - {Z_{OC}}^{-1} \right)^{-1}$$

$$R_s = \mathrm{Re}\left[Z_{Series}\right], C_j = \frac{1}{\left(L_{TML}\omega - \mathrm{Im}\left[Z_{Series}\right]\right)\omega} \tag{7.6}$$

The obtained C_j is equal to 23.3 fF and $R_s = 24.5\ \Omega$ with error percentages 3.5% and 0.7%, respectively, in comparison with the results of the simulated ADS lumped components.

Based on the results above, the analytical extraction technique can provide a good estimate of the total S_{11} based equivalent circuit. However, as the percentage error increases, a more complex RC network is needed to be synthesized in order to analyze the UTC-PD once the applied bias voltage is not sufficient to fully deplete the intrinsic region of the device or in the case where the waveguide structures suffer from a leakage on the substrate. In this case, and for verification purposes, one can also employ an analytical extraction method for frequency asymptotes ($f \to \infty, f \to 0$). For this analysis, robust values for all equivalent circuit parameters can be found for different bias values.

7.2.4 The Transimpedance Amplifier

The generated mm-wave signals at the output of the UTC-PD require amplification in order to be transmitted to the 5G end users. A common type of amplifier used in communication systems that require broad bandwidth and high sensitivities is the transimpedance amplifier (TIA).

A simplified TIA architecture is shown in Fig. 7.8. A UTC-PD is connected to a negative feedback amplifier. The TIA circuit is a current-voltage converter, amplifying the mm-wave signal from the photodiode as current, and converts it into a voltage so as to be compatible at the output with equipment that in most cases is designed to be matched to 50 Ω. An important metric for the gain of TIAs is the transimpedance gain (Z_T) that is calculated as the ratio between the output voltage (V_{out}) over the input current (I_{ph}). The term transimpedance stems from the fact that the current and voltage defining Z_T are measured on two different ports and provide broad bandwidth and high gain without compromising the signal to noise ratio – calculated as the ratio between the output voltage (V_{out}) over the input current (I_{ph})) [16]. Z_T can be calculated in Ω or dBΩ based on (7.7):

$$Z_T = \frac{V_{out}}{I_{ph}} \ (\Omega) \ , \ Z_T = 20 \log \left(Z_T / \Omega \right) \ (dB\Omega) \tag{7.7}$$

Furthermore, the input impedance (Z_{in}) of the TIA needs to be low in order to match the output of the UTC-PDs. Based on Fig. 7.8, Z_T and Z_{in} are calculated in (7.8) as

$$Z_T = -\frac{A}{A+1} R_f, \ Z_{in} = -\frac{1}{A} Z_T = \frac{R_f}{A+1} \tag{7.8}$$

where A is the open loop gain and R_f is the feedback resistance. While designing such amplifiers, in order to maximize the transimpedance, the gain of the open loop amplifier needs to be maximized. The higher the Z_T, the higher the match between the TIA and the UTC-PD. In the ideal case where A is infinite, the transimpedance depends only on the feedback resistor and $Z_{in} = 0$. Even though that is not feasible

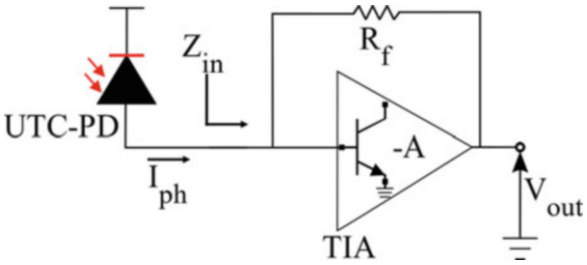

Fig. 7.8 An overview of the architecture combining a UTC-PD and a TIA supporting the generation of mm-waves

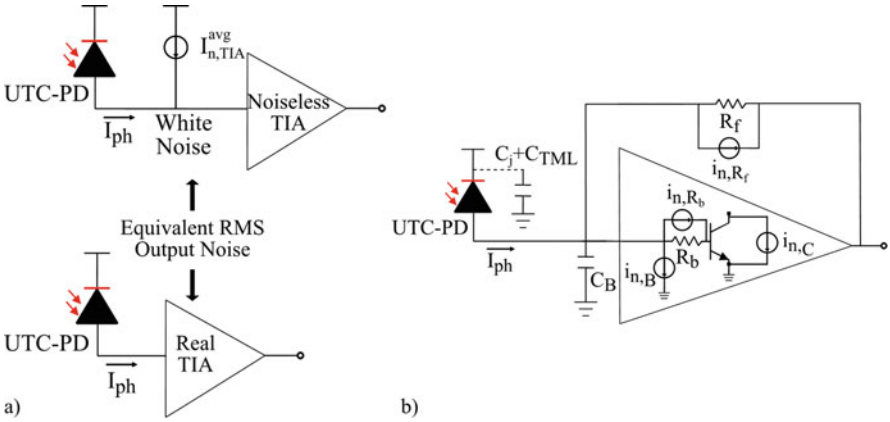

Fig. 7.9 (**a**) Definition of the input-referred noise current; (**b**) the noise sources of a TIA that includes HBT transistors

to be achieved, the abovementioned equations provide a general understanding on the basic function of this device.

7.2.4.1 Noise Analysis of TIAs

Concerning the noise calculations of TIAs, the input-referred noise current is a crucial parameter for this type of amplifier. As illustrated in Fig. 7.9a, this current is defined such that combined with a noiseless TIA, it is capable of reproducing the same noise levels as the actual (noisy TIA). The input-referred noise current can be measured in three different ways.

- Input-referred noise current PSD

  It is the power spectral density (PSD) $I_{n,TIA}^2$ of the input-referred noise current measured in pA^2/Hz and the noise current density ($\sqrt{I_{n,TIA}^2}$) in $pA/\sqrt{Hz}$. As illustrated in Fig. 7.9b, there is a multitude of noise sources contributing to $I_{n,TIA}^2$, including the thermal noise of the feedback resistance and the noise currents at the base and collector of the transistor of the open-loop amplifier [17, 18]. Therefore, this PSD is not white, and it cannot be provided by a single number [19]. A theoretical estimation of $I_{in,TIA}^2$ is given in (7.9).

$$I_{n,TIA}^2(f) \approx \frac{4kT}{R_f} + \frac{2qI_C}{\beta} + 2qI_C\frac{(2\pi C_{Tot})^2}{g_m^2}f^2 + 4kTR_b\left(2\pi C_j\right)^2 f^2 \qquad (7.9)$$

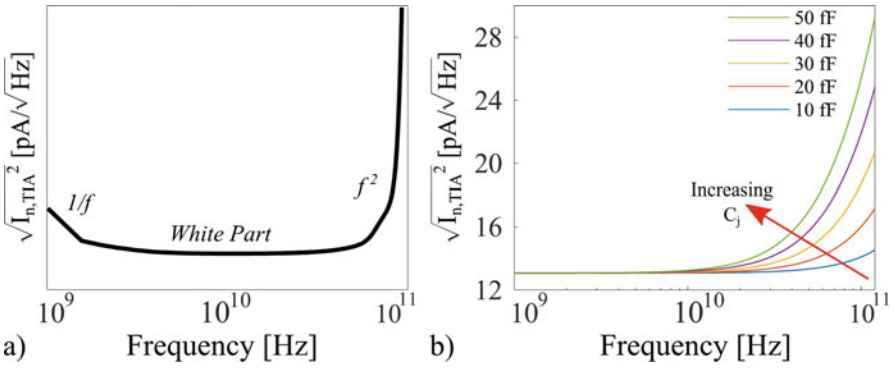

Fig. 7.10 (**a**) The typical curve of the noise current spectral density of a TIA; (**b**) the impact of the increasing junction capacitance of a UTC-PD to the $\sqrt{I_{n,TIA}^2}$

As shown in Fig. 7.10a, the $\sqrt{I_{n,TIA}^2}$ consists of a low-frequency part ($1/f$) due to the shot noise in the base and collector, white noise component, and two high-frequency (f^2) terms that are directly affected by the junction capacitance of the photodiode used since total input capacitance to the TIA is equal to $C_{Tot} = C_j + C_{TML} + C_B$.The dependence of C_j to $I_{n,TIA}^2$ is investigated in Fig. 7.10b for a single-feedback TIA based on (7.9) with R_f at the level of 250 Ω and β =30.2, I_C =9.4 mA, g_m =0.38 S, and R_b =40 Ω. By increasing C_j, the $I_{n,TIA}^2$ increases exponentially at higher frequencies. Thus, in the case where a combined module of a UTC-PD and TIA is designed, the C_j is required to be as low as possible.

- Input-referred RMS noise current

  It is an RMS value ($i_{n,TIA}^{rms}$) given by a single number (in nA or μA) and is extracted from the ratio of the RMS output voltage over the midband transimpedance value of the TIA [20]. The analytical equation is provided in

$$i_{n,TIA}^{RMS} = \frac{1}{Z_T}\sqrt{\int_0^{2\Delta f_1} v_{n,TIA}^{RMS} df} = \frac{1}{\overline{Z_T}}\sqrt{\int_0^{2\Delta f_1} \left|Z_T(f)^2\right| I_{n,TIA}^2(f) df} \tag{7.10}$$

where the term $\Delta f_1 = \frac{\pi}{2} f_{3dB}$ is the first-order-equivalent noise bandwidth of the TIA and is dependent on the f_{3dB} of the device.

- Averaged input-referred RMS noise current density

  This noise current definition ($I_{n,TIA}^{Avg}$) is measured in pA/√Hz and obtained by the ratio given by (7.11).

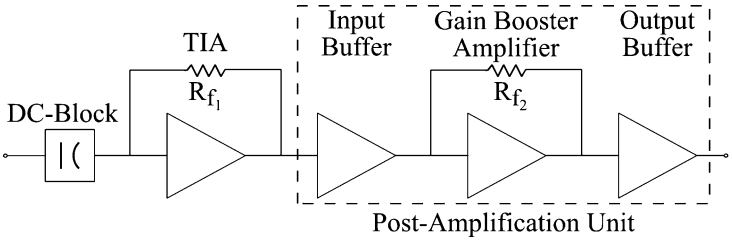

Fig. 7.11 The block diagram of a multistage TIA

$$I_{n,TIA}^{Avg} = \frac{i_{n,TIA}^{rms}}{\Delta f_1} \tag{7.11}$$

As presented in Fig. 7.9a, it is interpreted as the white noise source that needs to be connected to the input of a noise free TIA in order to reproduce the RMS output voltage noise of the real TIA.

The definitions analyzed in these sections provide valuable information on the results obtained in the TIA simulations.

7.2.4.2 Simulations on the Multistage TIA

Figure 7.11 shows a block diagram of the simulated multistage TIA design. At the RF input, a DC-block (capacitor) is added, prohibiting the reverse flow of the DC current toward the UTC-PD. A post-amplification unit after the first TIA further increases the total gain. It consists of an input buffer, a second transimpedance gain booster stage with a second feedback, and an output buffer driving the mm-wave antenna capable of transmitting mm-waves.

The amplifier circuit architecture is based on the common principle of inter-stage impedance mismatch where a transimpedance stage (TIS) is followed by a transadmittance stage (TAS). This method leads to the maximization of the device bandwidth [21]. The TIA is based and simulated on the FBH transferred-substrate InP-DHBT technology combining single- and double-finger transistors with emitter width equal to 500 nm [22]. As derived within the Fig. 7.12a, the simulated TIA achieves a high transimpedance (>75 dBΩ) with a 3 dB bandwidth within the V-band (>75 GHz).

The calculated noise current spectral density of the TIA in Fig. 7.12b follows the typical trend described in the previous section. Finally, the circuit exhibits a gain of 34 dB and a high output saturation power of 10 dBm once it is terminated to a 50 Ω load at both ends at an RF frequency of 60 GHz. The performance and properties of this device is capable of efficiently amplifying the mm-waves generated by the uni-travelling carrier photodiodes.

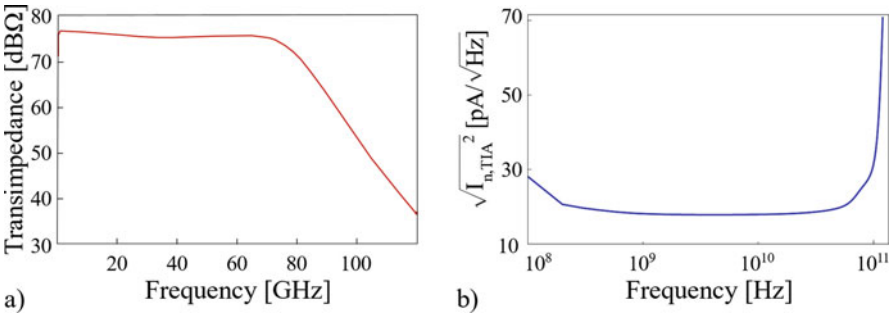

Fig. 7.12 (**a**) The transimpedance of the TIA as a function of frequency; (**b**) input current noise spectral density of the simulated TIA

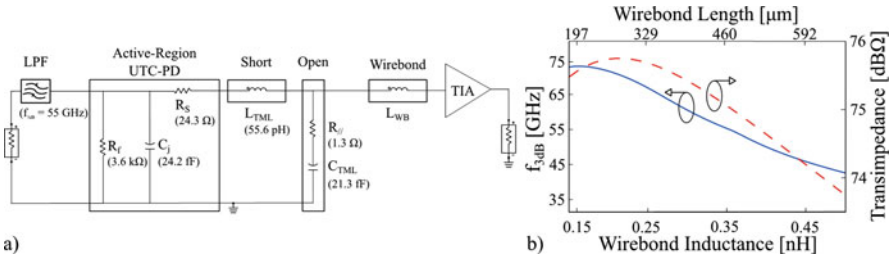

Fig. 7.13 (**a**) A 4 × 20 μm^2 UTC-PD interconnected with a TIA via a wirebond; (**b**) impact of wirebond length to the 3 dB bandwidth (blue) and transimpedance (red) of the total device

7.2.5 Co-simulation of the Interconnection Between UTC-PD and TIA

In Fig. 7.13a, the proposed TIA is co-simulated in ADS with the equivalent circuit of a measured 4 × 20 μm^2 waveguide UTC photodiode from III-V Lab (France) with a responsivity 0.79 A/W [23]. A low-pass filter (LPF) with a 3 dB bandwidth of 55 GHz is used in series to the circuit in order to simulate the transit time of the electrons within the device. This UTC-PD is interconnected with the TIA through a wirebond that is modeled as a lumped inductor.

In the blue curve of Fig. 7.13b, the inductance of the wirebond (L_{WB}) is swept over different values in order to analyze its impact on the f_{3dB} of the device. Also, in the upper x-axis of the diagram, the length of a straight gold wirebond is calculated with an assumed diameter of 17.78 μm [24]. With L_{WB} of 0.15 nH (or 197 μm), the maximum f_{3dB} is obtained at 73.1 GHz where the effect of gain peaking on the response of the component is observed [25]. Therefore, the poles originating from the DC-block and the parasitic capacitances of the UTC-PD that reduce the f_{3dB} are compensated by the L_{WB} [26]. Furthermore, the impact of the wirebond to the transimpedance exhibits a small variation (of approximately 2 dBΩ) over the

swept wirebond inductances. Thus, once the UTC-PD and the multistage TIA are simulated as one module, the co-integration process does not limit its frequency response.

These simulation results are very promising providing substantial input on the synthesis of a low-cost and low-energy consumption hybrid optical-electronic component that combined with integrated antenna elements can be replicated and will eventually fulfil one of the requirements that 5G poses which is massive deployment of numerous base stations within urban areas.

7.3 Optical Receiver Design for UDWDM-PON

Passive optical networks (PONs) are most commonly associated with the fiber to the x (FTTx) applications, where x = home, curb, or building. Currently deployed FTTx PONs, based on time division multiplexing (TDM) equipment, use only one wavelength and separate users in time domain where each optical network unit (ONU) can only transmit and receive signal at a specific time slot, and this will influence the system latency and system capacity. To increase the capacity to meet the increasing bandwidth demand for 5G, advanced techniques combined with wavelength division multiplexing are being investigated. Starting from the concept of Dense WDM (DWDM), implementing 40 channels at 100 GHz spacing or 80 channels with 50 GHz spacing, it is possible to further reduce the channel spacing using suitable technologies capable of 12.5GHz or even 6.25 GHz of spacing, introducing the notion of ultradense WDM (UDWDM). Allowing the use of over 256 channels, UDWDM finally enables the "λ-to-the-User" concept. The main challenge for UDWDM-PON is to make the deployment costs affordable to access users. The research emphasis is placed on cost-effective solutions in modulation formats selection, receiver design, and impairments compensation. Receivers based on coherent detection are able to choose the required wavelength by the local oscillator (LO) so as to achieve "colorless" ONU. However, the traditional coherent receiver is too complexed for PON application due to its expensive optical and electronic components. Simplified digital coherent receiver design starts to play an important role in the UDWDM-PON filed. Except for coherent, some proposals also suggest the use of direct detection (see Fig. 7.14), but colored ONU will place pressure on the wavelength management. PON requires enough power budget to support more users so as to reduce system cost, but the signal usually is subject to severe distortions, such as fiber dispersion-induced inter-symbol interference (ISI) and system bandwidth limitation, which become worse with the increase in system capacity. Additionally, when a semiconductor optical amplifier (SOA) is employed as a booster or pre-amplifier to increase the power budget, the nonlinearities due to the gain saturation of SOA will significantly degrade the signal quality. In the following sections, these topics will be discussed in detail.

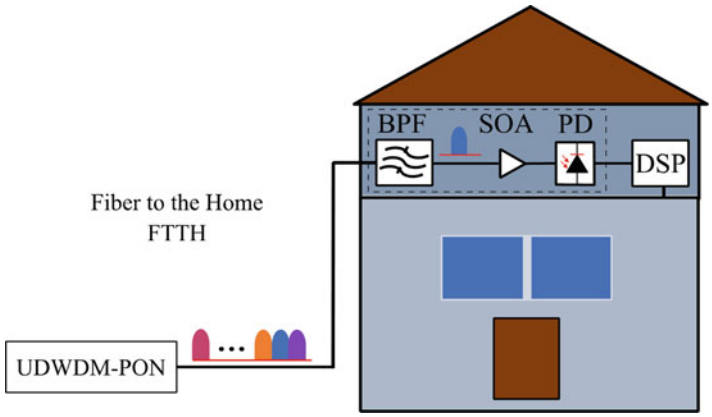

Fig. 7.14 A block diagram of UDWDM-PON for FTTH application

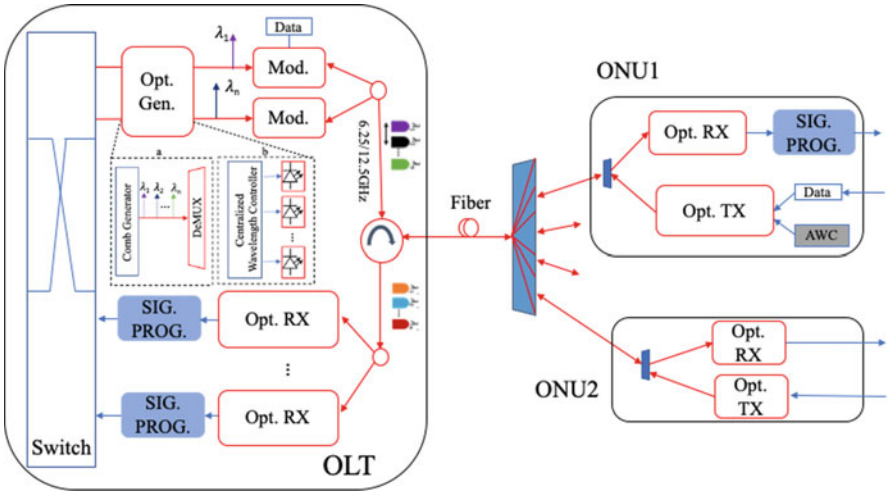

Fig. 7.15 System architecture of UDWDM-PON; inset: (**a**) Comb generator; (**b**) multiple lasers for optical carrier generation (*Opt Gen* Optical generator; *Mod* modulator; *SIG PROG* signal processing; *RX* receiver; *TX* transmitter; *AWC* automatic wavelength controller

7.3.1 Physical Architecture of UDWDM-PON

Figure 7.15 shows the basic physical architecture of UDWDM-PON system. The optical line terminals (OLTs) located in the central office are responsible for the data switching in the whole network as well as for the connection with the upper network layer.

However, the ONUs near to the user side will receive data and send users' request. In the downlink, the sending data is firstly converted form electrical to the

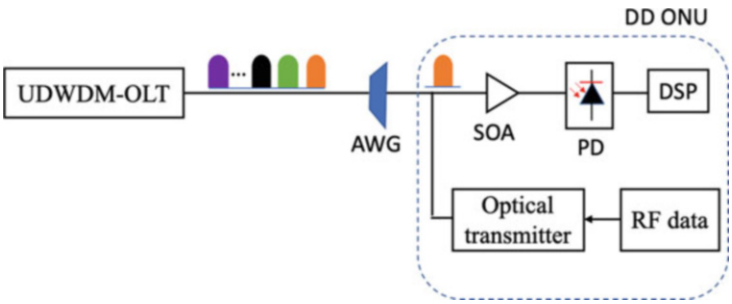

Fig. 7.16 A block diagram of DD-based ONU for UDWDM-PON

optical domain. The optical carriers are densely spaced and are initially generated either by using multiple laser sources or a comb source as show by inset (a) (b). For the multiple laser sources, a centralized wavelength locker combined with a high-performance thermoelectric cooler prohibiting the frequency drift of the sources [27] is employed. In terms of the comb source, it can simplify the tone generation, but an extra demultiplex needs to be added into the OLTs to separate the tones of the comb. The wavelength distance should follow the ITU-T recommendation G.694.1 which is lower to 6.25GHz and 12.5GHz [28]. The generated optical signal will be modulated with electrical signals. After wavelength multiplexing, the signal will travel through an optical circulator enabling bidirectional transmission in the fiber.

In the next step, a UDWDM splitter dictates the separation of signal to each ONU. Such a component can be an arrayed waveguide grating (AWG) separating the overall UDWDM signal to the specific ONU (see the configuration in Fig. 7.16).

In this case, a cost-effective receiver based on direct detection (DD) can be deployed. Since commercial avalanche photodiodes (APD) with high receiver sensitivity is costly and its bandwidth is much lower compared to photodiode (PD), SOA combined with PD is another option for a DD receiver which can keep a similar receiver sensitivity and sufficient bandwidth for high-speed transmission. The problem with the SOA is the nonlinear pattern effect due to the gain saturation; therefore, digital signal processing (DSP) will be employed to compensate this distortion; the detailed discussion will be presented in the following section.

If a coherent receiver is used in the ONU, then a simple passive splitter will first split the optical signal to all ONUs, and the LO in the RX will help detect the target wavelength (see the configuration in Fig. 7.17).

To simplify the structure of the ONU, some of the tones from the OLT can also feed the optical transmitters of the ONUs as the upstream carrier. Note that the traditional coherent receiver is too complicated for PON applications; hence some simplified coherent receiver designs are proposed which will be discussed in the following section. To demodulate the signal and compensate the system impairments, a DSP module will be implemented. For the uplink, the received information from the ONUs travels through the combiner and the circulator. Once more, the received signals will be demultiplexed, and then the data will be extracted

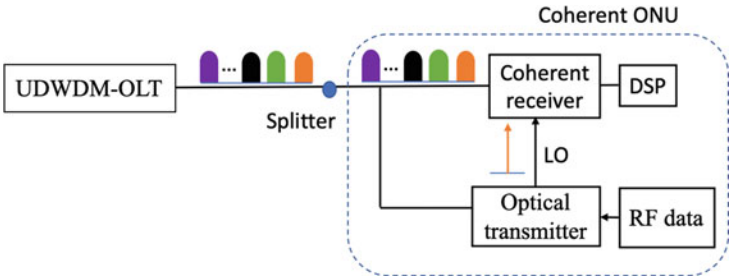

Fig. 7.17 A block diagram of coherent ONU for UDWDM-PON

from an optical receiver. Some signal processing module will help compensate the system impairments.

In order to achieve the power budget required to perform UDWDM, and also reduce the system cost as much as possible, there is a need to further improve the overall performance of some key parameters of the whole system such as the modulation format and receiver design. In the subsequent section, cost-effective receiver design and the modulation formats choices will be presented.

7.3.2 Receiver Design in the ONU: Direct Detection or Coherent

DD is a simple method which uses a single PD to achieve electrical signal recovery from the optical signal. During the past 20 years, direct detection has been employed as a common solution in the optical access network due to its cost-efficient and low-power consumption features. By using simple NRZ modulation formats, a maximum capacity up to 100 Gb/s can be achieved based on direct detection in a combination with time and wavelength-division multiplexed (TWDM) system [29, 30], which is currently considered a highly relevant topic by the IEEE 802.3ca task force. DD means the receiver can use a single PD or APD to detect signal and recover the amplitude of the signal. A demonstration shown in Fig. 7.18 [31] employs DD in the UDWDM system. An AWG filter with a channel spacing of 12.5 GHz at the remote node is used to distribute the wavelengths to the end users, "coloring" the whole network. Colored network means each ONU requires a specific wavelength which will require spectrum management and increase the system cost. Since PD typically has relative lower sensitivity compared to APD, other passive optical components used in the system will increase insertion loss, and thus additional optical amplifiers will be required to increase the system loss budget.

To enable flexible network operation by allowing colorless operation of the ONU without AWG or tunable optical filters in the ODN, receivers based on coherent

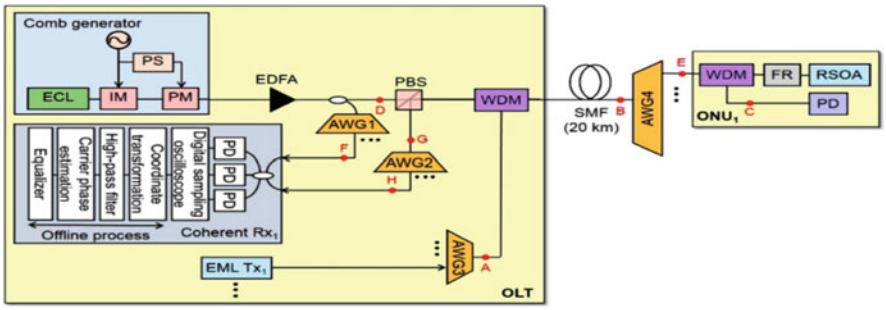

Fig. 7.18 Configuration of the proposed 12.5-Gb/S, 12.5-Ghz spaced UD-WDM PON based on DD [30]

rather than direct detection can be deployed, selecting a wavelength channel simply by tuning the LO laser to the wavelength of the downstream channel of interest. Fine wavelength selectivity in coherent WDM-PONs enables the use of (ultra-) dense wavelength spacing while avoiding the requirement for sophisticated optical wavelength filtering. Recent demonstrations of this technique include 10 Gbps/λ transmission in a 5 GHz grid [32] and 3.75 Gbps/λ and 1 Gbps/λ in a 2.5GHz grid [33, 34]. In addition to this key advantage, coherent receivers offer significantly higher receiver sensitivities in comparison to DD receivers [34, 35]. This will be a major advantage in future PON technologies, operating at multi-Gb/s per subscriber, and offering higher loss budgets, enabling higher split ratios (i.e., increased number of users) and longer reach. The high receiver sensitivity enables high-power budgets that can be shared arbitrarily between reach and split ratio depending on the network requirements. High split ratios reduce per-user costs since more end users can be supported in an access network using a single feeder fiber. Moreover, the optical amplitude, phase, and polarization can all be encoded with information, so it can allow a greater increase in the data rate without putting too much pressure on the electrical devices. Second, an optical coherent detection scheme is a linear detection where transmission impairments can be completely compensated by using DSP, so a higher receiver sensitivity can be obtained. In all, coherent detection is a way that can take advantage of the full potential of fiber transmission in a flexible way. Although coherent technology offers significant advantages, the complexity and high cost of conventional intradyne digital coherent receivers have prevented their use in PON applications. Thus, simplified coherent technology can play an important role in future access and mobile backhaul PONs.

It is acknowledged that if polarization-independent reception can be realized while avoiding the requirement for an optical polarization tracking unit in the coherent receiver, the complexity can be significantly reduced. To date, there are six reported low-complexity polarization-independent coherent receiver architectures employing various techniques; a comparison between the different designs is presented in [36]. The Alamouti receiver [37, 38] as depicted in Fig. 7.19 and Fig. 7.20 is a coherent receiver which detects an Alamouti polarization-time block-

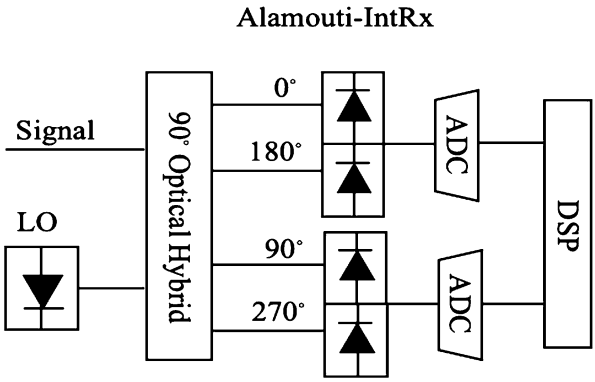

Fig. 7.19 Alamouti intradyne receiver [36]

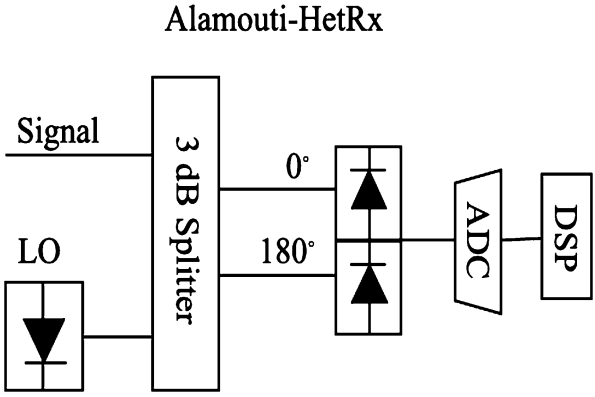

Fig. 7.20 Alamouti heterodyne receiver [37]

coded (PTBC) signal, requiring a dual-polarization modulator to avoid the need for an optical polarization tracking unit in the receiver. Although it introduces 50% redundancy due to the replication of the transmitted symbols, it leads to a significant simplification in the design compared to the conventional polarization- and phase-diverse intradyne (PPDI) coherent receiver.

In the 1980s, Glance has proposed a polarization-independent optical heterodyne receiver [39], referred to as Glance/Cano-HetRx, which has been demonstrated in a 1.25 Gb/s transmission system first [40] and, more recently, in real-time operation using 10 Gbps OOK signal [41]. The receiver consists of a 3 dB coupler and a polarization beam splitter (PBS) followed by two single-ended PDs, each detecting a polarization component, as shown in Fig. 7.21.

Following signal detection, the photocurrents at intermediate frequencies are first filtered, demodulated separately, and, finally, summed to obtain a baseband signal. Due to its capability of detecting two polarization modes, the detection process is independent of the polarization state of the received optical signal.

Moreover, Cano proposed in [42, 43] an alternative low-complexity coherent receiver design for use in ONUs, achieving polarization-independent detection employing a polarization scrambling (PS) method, in which every symbol is

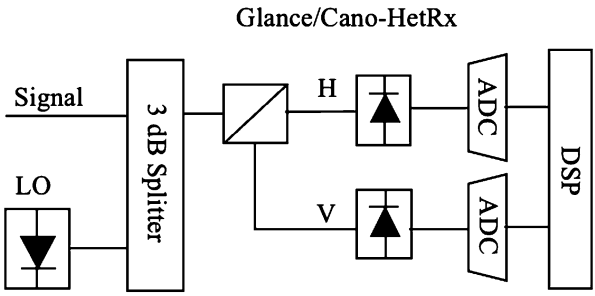

Fig. 7.21
Glance/Cano-HetRx [38]

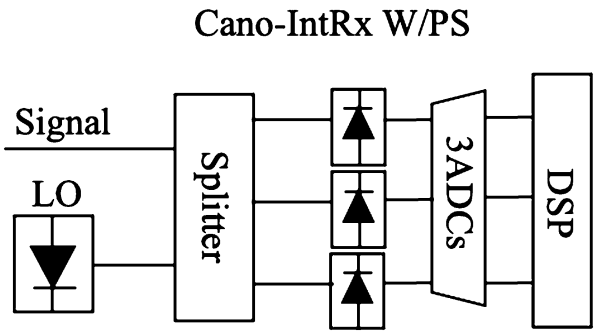

Fig. 7.22 Cano-IntRx [41]

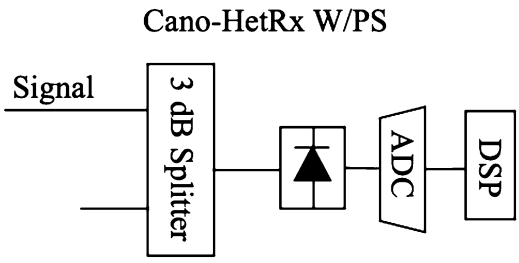

Fig. 7.23 Cano-HetRx [42]

transmitted twice, in orthogonal polarization states during two time slots. The Cano-IntRx consists of a symmetric 3 × 3 (1:1:1) coupler (using only two input ports) followed by three single-ended PDs and three ADCs, as illustrated in Fig. 7.22. In contrast, the Cano-HetRx has a simpler architecture which comprises a 3 dB coupler and a single-ended PD followed by a single ADC, as depicted in Fig. 7.23.

Ciaramella has proposed a simplified coherent receiver achieving polarization-independent reception in [44]. It employs a PBS and a symmetric 3 × 3 coupler (utilizing all three ports) followed by three single-ended PDs, as depicted in Fig. 7.24 [43]. The LO laser is separated into two orthogonal states of polarization (denoted as "H" and "V") using a PBS, and subsequently, they are mixed with the signal component. The output photocurrents are passed through the DC-blocks and then squared and summed to obtain the baseband signal. Finally, the signal is

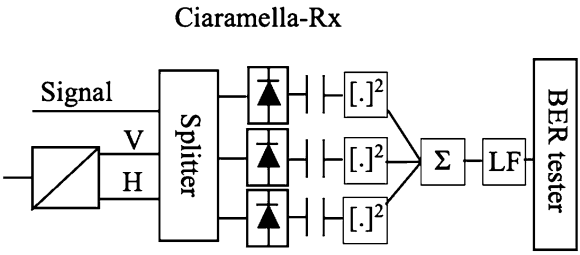

Fig. 7.24 Ciaramella Rx [43]

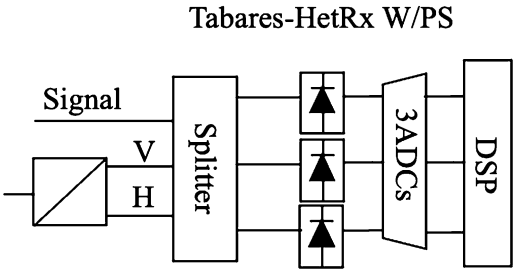

Fig. 7.25 Tabares HetRx [44]

low-pass filtered before being input to a clock and data recovery circuit. The key advantage of the Ciaramella-Rx is that it requires only simple analog processing, i.e., there is no need for an ADC or DSP. However, this receiver design is limited to amplitude-shift keying (ASK) (e.g., OOK or 4-PAM) signaling, and its tolerance to chromatic dispersion is lower than the other proposed receivers since the receiver linearity is lost due to squaring operation after the detection. A further disadvantage of this approach is that the receiver requires a large signal-LO frequency offset (0.9 × symbol rate (fb)) to avoid interference from low-frequency components of the directly detected signal. Therefore, the use of a single laser in the ONU, operating as both the upstream signal source and the downstream signal LO, is not possible.

To regain the phase diversity, Tabares [45] modified the Ciaramella-Rx by replacing the squaring operation with the linear combination of the three output photocurrents to remove the direct detection terms (identical to Cano-IntRx w/PS) while employing the same optical front-end design as the Ciaramella-Rx, as shown in Fig. 7.25 [44]. Although the linear operations to cancel direct detection terms can be performed in the analog domain, it is desirable for it to be performed digitally, requiring three ADCs to achieve high receiver sensitivity.

Simulations results are shown in Fig. 7.26a, b, where BER vs Received Power and bit error ratio (BER) vs photons per bit (PPB) curves are drawn for above proposed architectures and modulation formats. Additionally, Table 7.2 [36] presented a comparison between the proposed receiver, focused on spectrum efficiency, PPB, bit rate, and, of course, sensitivity.

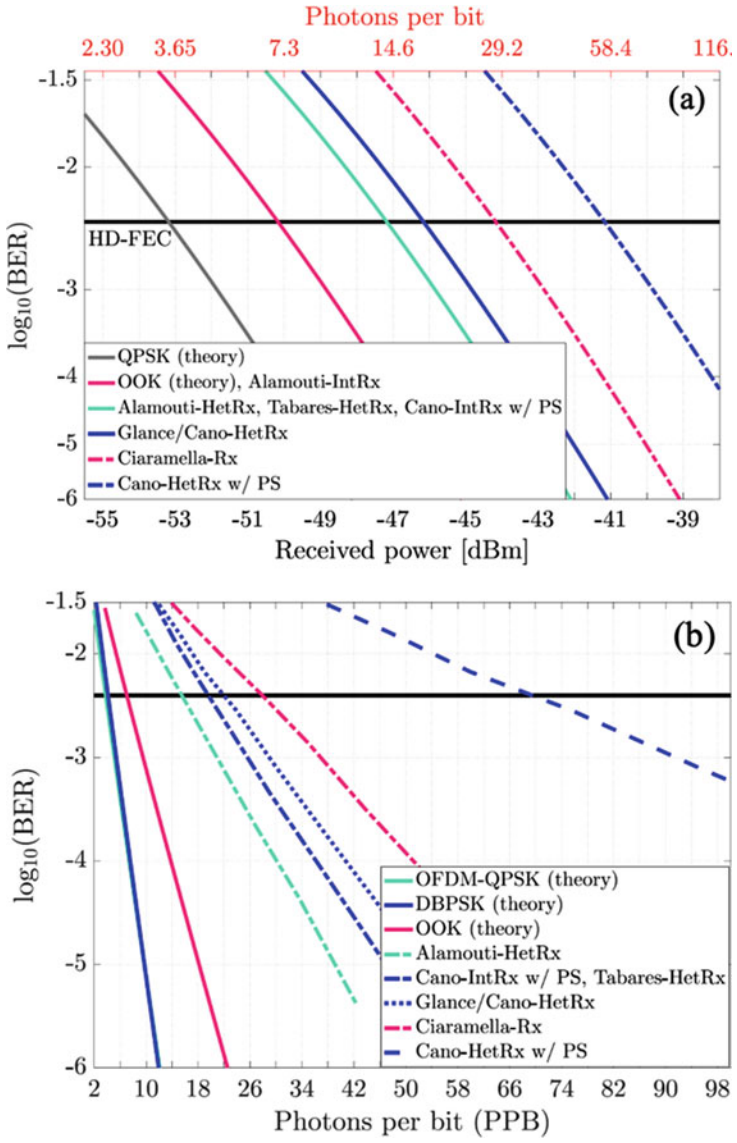

Fig. 7.26 (**a**) BER vs received power, (**b**) BER vs PPB

7.3.3 Modulation Format Choices for UDWDM-PON

It is well acknowledged that the complexity of conventional (dual-polarization digital) coherent receivers has so far prevented their introduction into access networks. Thus, low complexity in coherent receivers is needed. On the other

Table 7.2 Comparison of coherent receivers achieving polarization independent detection

Simplified coherent Rx	Modulation (SE [bis/s/Hz])	B2B req. PPB in sim.	Exp. sensitivity/bit rate [PPB]/[Gbps]	Distance [km]
Ciaramella-Rx	OOK	28	246.8/10	105
Tabares-HetRx	DBPSK	19.5	78.5/1.25	50
Cano-IntRx w/PS	DBPSK	19.5	78.5/1/25	50
Cano-HetRx w/PS	DBPSK	69.3	197.4/1.25	50
Glance/Cano-IntRx	DBPSK	22	123.6/10	25
Alamouti-HetRx	AC-OFDM QPSK	15.5	58/10.7	108
Alamouti-HetRx	AC-OFDM 16QAM	36.5	230/21.4	38

hand, using power-efficient modulation formats is not only very attractive in the challenged power budget of PONs but also one of the most efficient ways to achieve higher data rates, better spectrum efficiency, and thus improved receiver sensitivity.

Discrete multitone (DMT), NRZ, EDB, and M-PAM are widely used as modulation formats in the direct detection PON system. DMT is a multicarrier modulation technique that uses the discrete Fourier transform (DFT) to divide the channel into several sine-shaped orthogonal sub-channels, which might be a promising technology for next-generation PONs while still using low-bandwidth optical components. The principle of the DMT transmitter and receiver is shown in Fig. 7.27. Since DMT has the benefit of loading symbols on subcarriers with different modulation formats depending on the quality of the subcarrier, it is able to realize high spectral efficiency and is robust to spectral deficiencies. Additionally, the DMT time domain signals are real, permitting more cost-effective IMDD (intensity modulation direct detection). Another feature DMT provides is flexibility and increased chromatic dispersion (CD) tolerance. However, it was shown that its high linearity requirements make it hard to outperform EDB and PAM-4 at the same rate for the same receiver sensitivity.

In most optical communication systems, NRZ has been the reference choice for decades due to the inherent simplicity of the electrical components. However, while still considering the IMDD scenario which is desirable for cost-effective applications like PONs, more spectrally efficient modulation formats like EDB and PAM4 are available when multiple amplitude levels are used. A comparison between these multilevel formats can be shown in Table 7.3.

Once a coherent receiver is applied in the UDWDM system, several coherently detected modulation formats can be adopted, namely, dual-polarization quadrature phase-shift keying (DP-QPSK), polarization-switched (PSwitch) QPSK, 4- and 16-pulse position modulation (PPM), and 2- and PAM4 (pulse amplitude modulation).

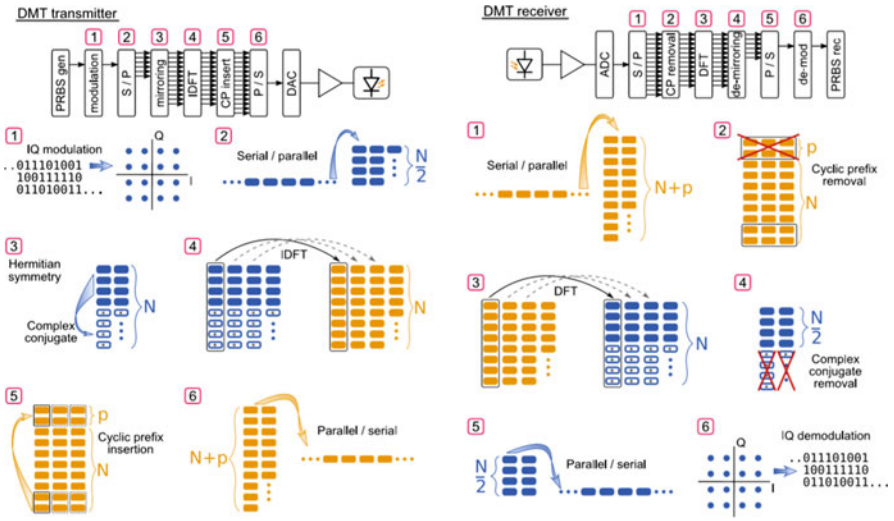

Fig. 7.27 DMT transceiver and receiver

Table 7.3 Comparison between modulation formats [46]

Modulation format	Sensitivity	Complexity	Required bandwidth	Dispersion tolerance
NRZ	√ √ √	√ √ √	√	√
NRZ-EDB	√ √	√ √	√ √	√ √
EDB	√	√ √	√ √ √	√ √
PAM4	√	√	√ √ √	√ √ √

A detailed comparison of these formats in terms of power efficiency is shown in [36]:

- PPM: If high sensitivity is the absolute primary requirement (neglecting the spectral efficiency), high-order M-PPM (e.g., $M \geq 16$) is a clear choice; however, it requires an M-fold increase in bandwidth compared to OOK (2-PAM).
- 4-PAM: On the other hand, 4-PAM offers double the information per symbol compared to OOK but requires approximately three times the number of PPBs.
- PSwitch-QPSK: When coherent detection using the conventional PPDI coherent receiver is considered, PSwitch-QPSK stands out as having the lowest required number of PPBs.
- DP-QPSK: PSwitch-QPSK requires 0.6 fewer PPBs than DP-QPSK at the expense of offering 25% lower spectral efficiency. Thus, a trade-off between sensitivity and optical/electrical bandwidth requirements for the targeted capacity needs to be evaluated.
- QPSK: if the polarization diversity is sacrificed to implement a low-complexity coherent receiver, the implementation of PSwitch-QPSK is not possible, whereas single-polarization QPSK might be a reasonable choice.

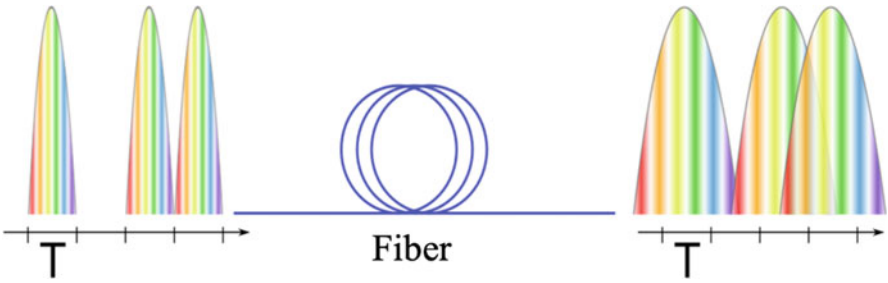

Fig. 7.28 Inter-symbol interference caused by pulse spreading over dispersive fiber

7.3.4 Optical Impairments and Mitigation Strategies in UDWDM-PON

The required increase of bit rate and reach of PONs poses new challenges on the physical layer design in order to meet the desired performance in a cost-effective way. Performance limitations in optical communication systems are due to both optoelectronic components and the optical fiber through which the signal propagates. In this section, the aspects most relevant to PONs are introduced and discussed, while factors that have a significant impact on higher capacity systems are omitted.

7.3.4.1 Chromatic Dispersion

In an optical communication system, dispersion is the dependence of the group velocity on the signal wavelength or on the propagation mode. Dispersion generally causes broadening in time of a light pulse as it propagates along the fiber as shown in Fig. 7.28. The spreading out of the pulse causes ISI (Inter Symbol Interference) which introduces distortions and limits the data rate and maximum length of the optical link.

Chromatic dispersion can be addressed with optical or electronic compensation at the receiver or at the transmitter. Optical compensation, which makes use of dispersion compensating fiber (DCF) or fiber Bragg gratings (FBGs) [47], is effective but requires bulky components and also has to be dimensioned to every specific link to enable optimum performance, making it unsuitable for a point to multipoint networks with an asymmetric physical structure. Besides, optical filtering [48] based on delay interferometer (DI) can compress the chirp of the modulator and then increase the tolerance of dispersion.

Electronic compensation, on the other hand, can provide reduced footprint and high flexibility and can harness the progress in complementary metal-oxide-semiconductor (CMOS)-based DSP technology with potential advantages both in terms of costs and scalability. For a direct detect receiver, feed-forward equalizer

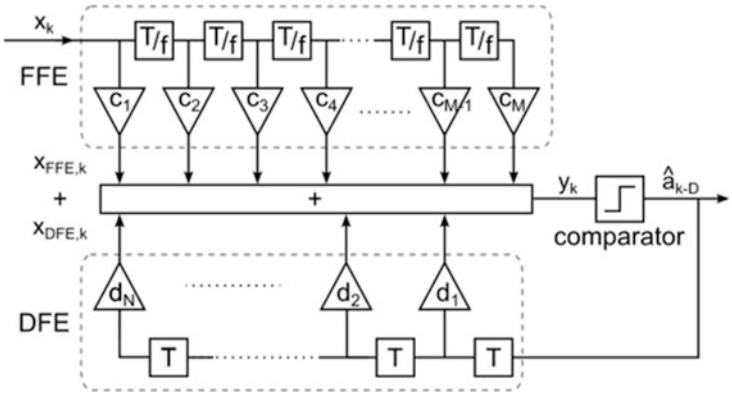

Fig. 7.29 Schematic of linear equalizer with FFE and DFE where delay blocks and tap coefficients are visible

(FFE) and decision feedback equalizer (DFE) are normal equalizers which use a tapped-delay line approach to compensate for ISI whose interference spreads over multiple symbols periods; a simple block diagram of the FFE and DFE is shown in Fig. 7.29.

7.3.4.2 Optical SOA Pattern Effect and Compensation with Neural Network

As mentioned above, the DD receiver can reduce the complexity of ONU. In order to improve the sensitivity of the DD receiver, a pre-amplifier is typically used before the PD. The associated gain saturation will degrade signal quality. Gain saturation is a phenomenon that originates from the dependence of the amplifier gain, G, on the input power of the input signal, $P_{S,in}$. When this value gets close to the amplifier saturation power, P_S, the gain will be reduced. The amplifier gain is defined as the ratio between the output and input power of the signal

$$G = \frac{P_{out}}{P_{S,in}} \tag{7.12}$$

The power of the signal propagating through the amplification medium can be expressed as

$$P(z) = P_{s,in} e^{gz} \tag{7.13}$$

where g is the material gain. After derivation, it can be expressed as

$$\frac{dP(z)}{dz} = gP(z) \tag{7.14}$$

The material gain, g, can be expressed as a function of P_s and the small signal gain g_0, [7]

$$g = \frac{g_0}{1 + \frac{P}{Ps}} \tag{7.15}$$

and hence

$$\frac{dP(z)}{dz} = \frac{g_0 P(z)}{1 + \frac{P}{P_s}} \tag{7.16}$$

By integrating this equation over the amplifier length, the following relation for the large-signal amplifier gain is obtained:

$$G = G_0 e^{\left(-\frac{G-1}{G} * \frac{P_{out}}{Ps}\right)} \tag{7.17}$$

The equation shows that the amplification factor G decreases from its unsaturated value G_0 when P_{out} becomes comparable to P_s. A useful metric commonly used is the output saturation power, which is defined as the output power for which the amplifier gain is reduced by a factor of 2, or 3 dB, from its unsaturated value G_0.

SOAs suffer from carrier depletion-induced saturation. When working in the saturation regime, the SOA becomes nonlinear causing a number of effects to occur including SPM, XPM, FWM, cross-gain modulation, and self-gain modulation. When an SOA amplifies a high-intensity modulated signal, self-gain modulation can lead to a serious waveform distortion commonly referred to as patterning effect (see the eye diagram performance in Fig. 7.30). As a kind of nonlinearity impairment induced by gain saturation, pattern-dependent effect can be mitigated by the nonlinearity compensation DSP at the receiver end.

In recent years, neural network (NN) has become very popular and has shown effective application in the fields of optical performance monitoring and nonlinearity equalization. It can be proved that an NN can fit and express any function if it has at least one hidden layer and enough hidden nodes [50]. Therefore, it is possible to use NN to compensate the nonlinearity from SOA. An experiment demonstration is conducted to verify the effectiveness of NNs – the setup is shown in Fig. 7.31. At the transmitter side, the 25 Gbaud PAM-4 downstream signal is generated by a digital-to-analog converter (DAC) working at 65 GSa/s with the 3 dB analog bandwidth of 20 GHz. A commercial 18Gbps DML (Directly Modulated Laser) with 3 dB bandwidth of 10 GHz and a center wavelength of 1310 nm is employed. The DAC output is first amplified by a 23 dB electrical amplifier (EA) before driving the DML. Then, the 25 Gbaud PAM-4 optical signals are transmitted over up to 20 km SSMF with an average loss of 0.33 dB/km at 1310 nm. In order to support high

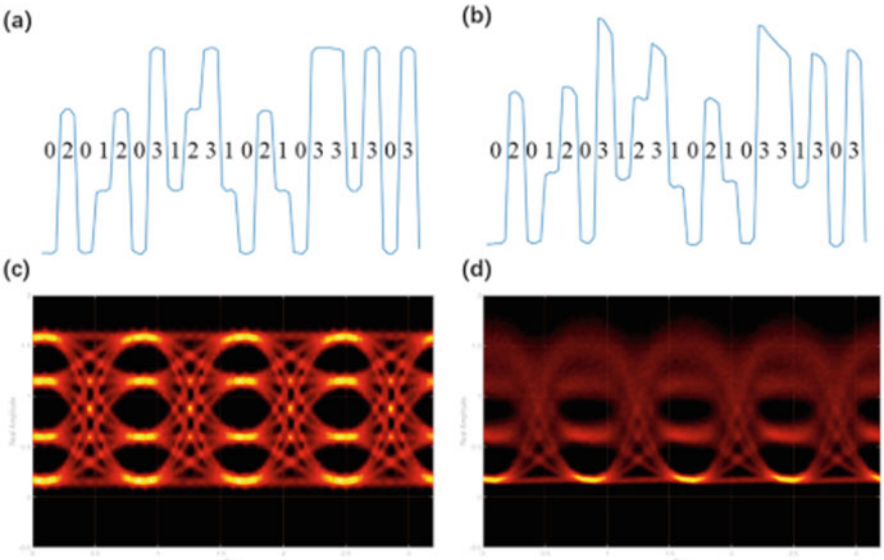

Fig. 7.30 The pattern effect of PAM-4 signal: (**a**) pulse shape and (**b**) eye diagram of the PAM4 signals without pattern effect; pulse shape (**c**) and eye diagram (**d**) of the PAM4 signals suffered from SOA-induced pattern effect [49]

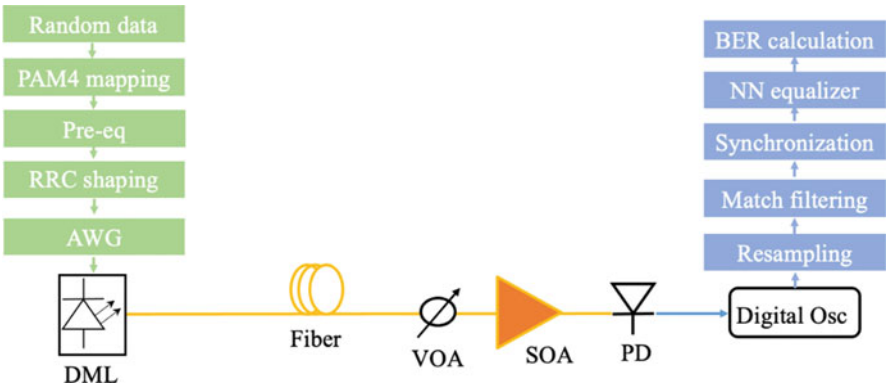

Fig. 7.31 The experimental setup of the NN based IM/DD system at O-band

link loss budget, an O-band SOA preamplifier is used at the receiver side before direct detection. A variable optical attenuator (VOA) is applied to emulate splitter loss and also test the SOA performance. A 50 GHz PD is chosen for this experiment to detect the signal. Then the output signal is captured by an 80 GSa/s oscilloscope with 20 GHz bandwidth and processed by offline DSP.

The DSP block at the transmitter sider (green flow) is shown in Fig. 7.31.

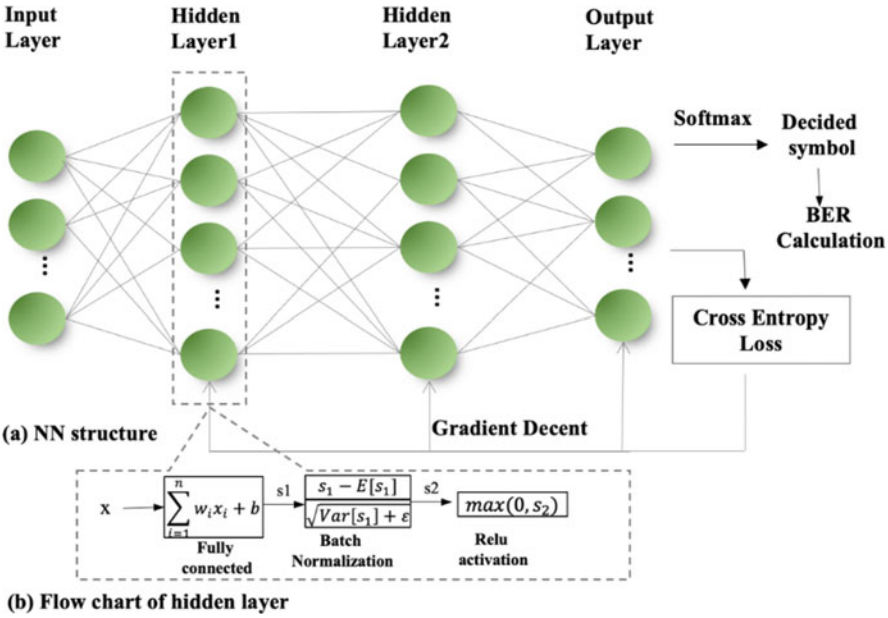

Fig. 7.32 The NN structure (**a**) and connection flow between hidden layer (**b**)

Random data generated by a Mersenne Twister are mapped into PAM-4 symbols with a length of 2^{15} and then upsampled to two times the data rate. The system performance with high baud rate will be seriously limited by the bandwidth limitation of the optoelectronic devices, such as the DAC, DML, and PD. The filtering effect from them can result in inter-symbol interference (ISI) and restrict the baseband signal bandwidth. Time-domain digital pre-equalization (pre-eq) and root-raised-cosine (RRC) filter with the optimal roll-off factor 0.15 are used to reduce the ISI caused by the bandwidth limitation. Next, the symbol sequence is resampled to match the sampling rate of the DAC.

The offline DSP block at the receiver side is shown by the blue flow. The captured offline data is first resampled to 1-sps with the matched filter, and then synchronization is applied to remove the time jitter and extract the sending data. Afterward, a full connected NN equalizer is used to reduce the linear and nonlinear impairments. The structure of the NN-based equalizer we apply in this work is shown in Fig. 7.32.

It is a four-layer network, containing two hidden layers. The circles denote the nodes, also known as neurons. It is a fully connected network, in which the input layer has 57 nodes; hence, the network requires 57 consecutive sampled symbols as input for a judged symbol. Each hidden layer has 128 nodes, while the output layer has 4 nodes, corresponding to the 4 symbols of PAM4 mode. The nonlinear activation function of the hidden layers is rectified linear unit (ReLU) used for nonlinear transformations, which is expressed as follows:

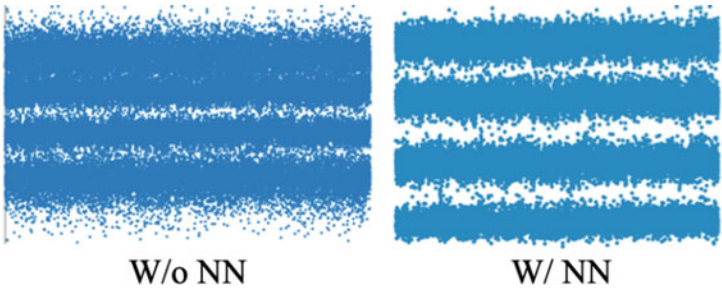

Fig. 7.33 Power-level distribution of received time domain signal with and without NN

$$y = \max(0, x) \tag{7.18}$$

The activation of output layer is softmax which is able to enforce the features to the range of (0, 1). The softmax function is expressed as follows:

$$y_j = \frac{e^{x_i}}{\sum_{j=1}^{N_{class}} e^{x_j}} \tag{7.19}$$

where x and y are input and output feature maps of the softmax function, i and j are the indexes of the neurons, N_{class} is the number of classes which is set as 4 considering the four levels of PAM4 signal, and y_j is the predicted probability of an observation belonging to jth class. The length of the whole data set is 100,000, 50,000 symbols for training and 50,000 symbols for the final test. The final performance is evaluated based on the BER of the test data set.

As mentioned earlier, the higher the input power to the SOA, the pattern effect due to the gain saturation will be more serious. We first set the input power to SOA as −1 dBm and compare the signal quality before and after NN equalization. The power-level distribution of the received time domain PAM4 signal is shown in Fig. 7.33.

The pattern effect will cause jitters for PAM symbols with higher power. Thus, the signals influenced by the pattern effect will be asymmetrical in the time domain. The third and fourth levels of the PAM-4 signals are overlapped. After employing the NN equalizer, the overlap induced distortion will be improved. We also compare the performance between FFE and NNs. As we can see from the result in Fig. 7.34, with the increase in input power, the BER will be improved first due to the increased signal-to-noise ratio (SNR).

However, once the power goes beyond −10 dBm, the FFE is not able to further improve the BER performance due to the nonlinearity introduced from the SOA. On the contrary, the NN-based equalizer can significantly improve the BER; therefore, we conclude that the SOA-induced pattern effect can be well addressed by NN.

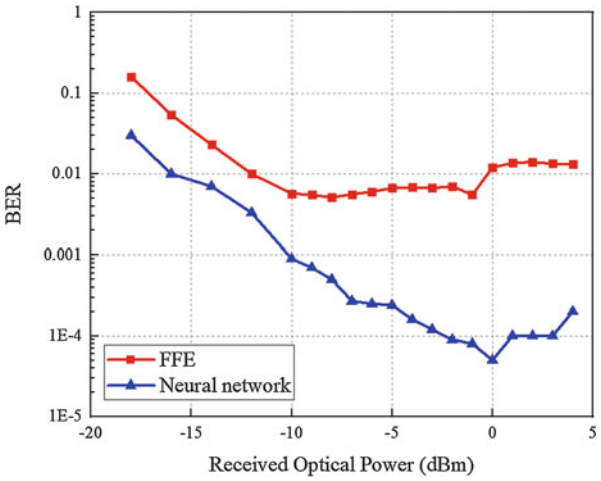

Fig. 7.34 BER versus the input power into the SOA of 50G PAM4 signal transmission over 20 km SMF at O-band

7.4 Conclusion

This chapter provided new insights into the design of future emerging 5G base stations and FTTH terminals that incorporate UDWDM-PONs for enabling high-capacity backhauling.

The physical properties of UTC-PDs are explained, and an equivalent circuit model of the uni-travelling carrier photodiodes is obtained based on reflection coefficient parameter extraction. In addition, a multistage TIA design simulated on InP/InGaAs HBT technology is reported operating within the V-band and exhibiting high gain and high output powers. A co-simulation of these two devices is conducted synthesizing an optoelectronic mm-wave transmitter capable of generating and amplifying 5G NR signals. Finally, the wirebond between a simulated UTC-PD and the TIA does not significantly degrade the bandwidth of the device, making the proposed co-integrated mm-wave transmitter an ideal choice for the generation of mm-wave signals within the future 5G base stations interconnected with UDWDM-PONs.

For FTTH applications, two types of optical receivers based on coherent and direct detection, respectively, are introduced. PON is sensitive to the cost; therefore, the complexity and high cost of conventional intradyne digital coherent receivers have prevented their use in PON applications. Thus, a variety of simplified coherent receiver designs are introduced. On one hand, the combination of SOA used as pre-amplifier with PDs is proposed as a low-cost solution for the receiver in a DD ONU system.

In practical PON systems, different ONUs are dimensioned with different receiving powers to cater for the diverse distances to the OLT. Varied optical power into the SOA will induce nonlinear distortions to the signal. Therefore, NN is proposed at the receiver side to mitigate SOA nonlinearities generated within the optical signals. The performance of NN is experimentally investigated in an IM/DD

system with 50G PAM4 signals. After optimizing the convergence factor of the NN, the SOA nonlinearities can potentially be compensated leading to improved receiver dynamic range, making the proposed SOA/PD package an alternative for the future ONU design in the UDWDM-PONs system.

Acknowledgments This work was partially funded by EU through the projects 5G STEP FWD (no. 722429), 5G-PHOS (no. 761989), TERAWAY (no. 871668), and blueSPACE (no. 762055).

References

1. Chin, W. H., Fan, Z., & Haines, R. (2014). Emerging technologies and research challenges for 5G wireless networks. *IEEE Wireless Communications, 21*(2), 106–112.
2. Konstantinou, D., et al. (2020). 5G RAN architecture based on analog radio-over-fiber fronthaul over UDWDM-PON and phased array fed reflector antennas. *Optics Communications, 454*, 124464.
3. Konstantinou, D., Morales, A., Rommel, S., Raddo, T. R., Johannsen, U., & Monroy, I. T. (2019). Analog radio over fiber fronthaul for high bandwidth 5g millimeter-wave carrier aggregated OFDM. In *International conference on transparent optical networks*, 2019, Vol. 2019-July.
4. Rommel, S., Olmos, J. J. V., & Monroy, I. T. (2017). 15Gbit/s duobinary transmission over a W-band radio-over-fiber link. In *Proceedings* – 2016 *advances in wireless and optical communications,* RTUWO *2016*, 2017, pp. 197–200.
5. Rommel, S., Morales, A., Konstantinou, D., Raddo, T. R., & Monroy, I. T. (2018). MM-wave and THz analog radio-over-fiber for 5G, wireless communications and sensing. In *Optics InfoBase conference papers*, 2018, Vol. Part F123-.
6. Johannsen, U., et al. (2019). ARoF-Fed antenna architectures for 5G networks. In 2019 *Optical fiber communications conference and exhibition, OFC 2019 – Proceedings*.
7. Agrawal, G. P. (2011). *Fiber-optic communication systems* (4th ed.).
8. Erman, M., et al. (1991). Optical circuits and integrated detectors. *IEE Proceedings. Part J, Optoelectron, 138*(2), 101–108.
9. Xu, Z., & Gao, J. (2017). Semi-analytical small signal parameter extraction method for PIN photodiode. *IET Optoelectronics, 11*(3), 103–107.
10. Maloney, T. J., & Frey, J. (1977). Transient and steady-state electron transport properties of GaAs and InP. *Journal of Applied Physics, 48*(2), 781–787.
11. Othman, M. A., Taib, S. N., Husain, M. N., & Napiah, Z. A. F. M. (2014). Reviews on avalanche photodiode for optical communication technology. *ARPN Journal of Engineering and Applied Sciences, 9*(1), 35–44.
12. Shimizu, N., Miyamoto, Y., & Ishibashi, T. (1999). Uni-traveling-carrier photodiodes. *Conference Proceedings – Lasers and Electro-Optics Society Annual Meeting-LEOS, 2*, 808–809.
13. Ito, H., Nagatsuma, T., & Ishibashi, T. (2007). Uni-traveling-carrier photodiodes for high-speed detection and broadband sensing. *Quantum Sensing and Nanophotonic Devices IV, 6479*, 64790X.
14. Konstantinou, D., Caillaud, C., Rommel, S., Johannsen, U., & Tafur Monroy, I. (2020). Investigation of de-embedding techniques applied on uni-traveling carrier photodiodes. In *EuMiC*.
15. "Advanced Design System (ADS), ADS 2020.02, Keysight EEsof EDA, Keysight Technologies."
16. Razavi, B. (2008). Fundamentals of microelectronics. *Change, 13*, 1–4.

17. Paasschens, J. C. J., Havens, R. J., & Tiemeijer, L. F. (2003). Modelling the correlation in the high-frequency noise of (hetero-junction) bipolar transistors using charge-partitioning. In *Proceedings of the IEEE Bipolar/BiCMOS circuits and technology meeting*, 2003, pp. 221–224.
18. Meyer, R. G., & Blauschild, R. A. (1986). A wide-band low-noise monolithic transimpedance amplifier. *IEEE Journal of Solid-State Circuits, 21*(4), 530–533.
19. Tagami, H., et al. (2005). A 3-bit soft-decision IC for powerful forward error correction in 10-Gb/s optical communication systems. *IEEE Journal of Solid-State Circuits, 40*(8), 1695–1703.
20. Säckinger, E. (2005). Broadband circuits for optical fiber communication.
21. Rein, H. M., & Möller, M. (1996). Design considerations for very-high-speed Si-bipolar IC's operating up to 50 Gb/s. *IEEE Journal of Solid-State Circuits, 31*(8), 1076–1090.
22. Shivan, T., et al. (2019). A 175 GHz bandwidth high linearity distributed amplifier in 500 nm InP DHBT technology. In *IEEE MTT-S international microwave symposium digest*, 2019, Vol. 2019-June, pp. 1253–1256.
23. Achouche, M., et al. (2004). High performance evanescent edge coupled waveguide unitraveling-carrier photodiodes for >40-Gb/s optical receivers. *IEEE Photonics Technology Letters, 16*(2), 584–586.
24. Qi, X., et al. (1998). Fast 3D modeling approach to parasitics extraction of bonding wires for RF circuits. In *Technical digest – International electron devices meeting*, pp. 299–302.
25. Konstantinou, D. (2020). Simulation of an integrated UTC-photodiode with a high-speed TIA for 5G mm-wave generation. In *NUSOD*.
26. Chen, G., Yu, Y., Deng, S., Liu, L., & Zhang, X. (2015). Bandwidth improvement for germanium photodetector using wire bonding technology. *Optics Express, 23*(20), 25700.
27. Pachnicke, S. et al. (2014). First demonstration of a full C-band tunable WDM-PON system with novel high-temperature DS-DBR lasers. In *Optics InfoBase conference papers*.
28. International Telecommunication Union – ITU-T, "Rec. ITU-T G.694.1 (02/2012)," 2012.
29. Ji, H., et al. (2017, May). Field demonstration of a real-time 100-Gb/s PON based on 10G-class optical devices. *Journal of Lightwave Technology, 35*(10), 1914–1921.
30. Xue, L., Yi, L., Ji, H., Li, P., & Hu, W. (Jan. 2018). Symmetric 100-Gb/s TWDM-PON in O-band based on 10G-class optical devices enabled by dispersion-supported equalization. *Journal of Lightwave Technology, 36*(2), 580–586.
31. Shim, H. K., Kim, H., & Chung, Y. C. (2014). Practical 125-Gb/s, 125-GHz spaced ultra-dense WDM PON. *Optics Express, 22*(23), 29037.
32. Luo, M. et al. (2018). Demonstration of 10-Gb/s, 5-GHz spaced coherent UDWDM-PON with Digital signal processing in real-time. In *Optics InfoBase conference papers*, 2018, vol. Part F84-O.
33. Ferreira, R. M., Shahpari, A., Reis, J. D., & Teixeira, A. L. (2017). Coherent UDWDM-PON with dual-polarization transceivers in real-time. *IEEE Photonics Technology Letters, 29*(11), 909–912.
34. Smolorz, S., Gottwald, E., Rohde, H., Smith, D., & Poustie, A. (2011). Demonstration of a coherent UDWDM-PON with real-time processing. In *Optics InfoBase conference papers*.
35. Shahpari, A., et al. (2017). Coherent access: A review. *Journal of Lightwave Technology, 35*(4), 1050–1058.
36. Erkilinc, M. S., et al. (2018). Comparison of low complexity coherent receivers for UDWDM-PONs (λ-to-the-user). *Journal of Lightwave Technology, 36*(16), 3453–3464.
37. Shieh, W., Yi, X., Ma, Y., & Yang, Q. (2008). Coherent optical OFDM: Has its time come? [Invited]. *Journal of Optical Networking, 7*(3), 234–255.
38. Erkilinç, M. S., et al. (2016). Polarization-insensitive single-balanced photodiode coherent receiver for long-reach WDM-PONs. *Journal of Lightwave Technology, 34*(8), 2034–2041.
39. Glance, B. (1987). Polarization independent coherent optical receiver. *Journal of Lightwave Technology, 5*(2), 274–276.
40. Cano, I. N., Lerín, A., Polo, V., & Prat, J. (2014). Simplified polarization diversity heterodyne receiver for 1.25Gb/s cost-effective udWDM-PON. In *Optics InfoBase conference papers*.

41. Altabas, J. A., et al. (2018). Real-time 10Gbps polarization independent quasicoherent receiver for NG-PON2 access networks. In *Optics InfoBase conference papers*, 2018, Vol. Part F84-O.
42. Cano, I. N., Lerin, A., Polo, V., & Prat, J. (2015). Flexible D(Q)PSK 1.25-5 Gb/s UDWDM-PON with directly modulated DFBs and centralized polarization scrambling. In *European conference on optical communication, ECOC*, 2015, Vol. 2015-Novem.
43. Cano, I. N., Lerín, A., Polo, V., & Prat, J. (2014). Polarization independent single-PD coherent ONU receiver with centralized scrambling in udWDM-PONs. In *European Conference on Optical Communication, ECOC*, 2014.
44. Ciaramella, E. (2014). Polarization-independent receivers for low-cost coherent OOK systems. *IEEE Photonics Technology Letters, 26*(6), 548–551.
45. Tabares, J., Polo, V., & Prat, J. (2017). Polarization-independent heterodyne DPSK receiver based on 3×3 coupler for cost-effective udWDM-PON. In *Optics InfoBase conference papers*, 2017, Vol. Part F40-O.
46. Dalla Santa, M. (2019). *Next generation technologies for 100 Gb/s PON systems*. University College Cork.
47. Yi, L., Wang, X., Li, Z., Huang, J., Han, J., & Hu, W. (2015). Upstream dispersion management supporting 100 km differential reach in TWDM-PON. *Optics Express, 23*(6), 7971.
48. Li, Z., et al. (2014). Symmetric 40-Gb/s, 100-km passive reach TWDM-PON with 53-dB loss budget. *Journal of Lightwave Technology, 32*(21), 3389–3396.
49. Wang, K., Zhang, J., Zhao, L., Li, X., & Yu, J. (2020). Mitigation of pattern-dependent effect in SOA at O-band by using DSP. *Journal of Lightwave Technology, 38*(3), 590–597.
50. Nielsen, M. A. (2015). *Neural networks and deep learning*. Determination Press.